Journal of Biomechanics 84 (2019) 234–242

Contents lists available at ScienceDirect

Journal of Biomechanics

journal homepage: www.elsevier.com/locate/jbiomech
www.JBiomech.com

Three-dimensional collective cell motions in an acinus-like lumen

Peng-Cheng Chen [a], Shao-Zhen Lin [a], Guang-Kui Xu [b], Bo Li [a,*], Xi-Qiao Feng [a]

[a] Institute of Biomechanics and Medical Engineering, AML, Department of Engineering Mechanics, Tsinghua University, Beijing 100084, China
[b] Department of Engineering Mechanics, State Key Laboratory for Strength and Vibration of Mechanical Structures, Xi'an Jiaotong University, Xi'an 710049, China

ARTICLE INFO

Article history:
Accepted 3 January 2019

Keywords:
Cell mechanics
Collective cell migration
Three-dimensional lumen
Migratory mode

ABSTRACT

Collective cell migration is an essential process in embryo development, wound healing, inflammatory response, and cancer invasion. Although cell motions in two-dimensional (2D) monolayers have been studied previously, three-dimensional (3D) collective cell migration, which constantly occurs during embryogenesis such as the establishment of ducts and acini *in vivo*, remains elusive. In this paper, we develop a cell-based model incorporating cell mechanics and cell motility to address coherent cell motions in a spherical acinus-like lumen with different cell populations. It is found that the interplays between cell persistence, random fluctuation, and geometrical confinement may engender rich and novel migratory modes. In a 3D spherical lumen, two cells may undergo stripe-like or cross-circular coherent rotations, whereas multiple cells can form dynamic twisting or circulating bands, leaving sparse cells at the center or even a hollow cavity in the cell aggregate. The cell density is found to profoundly influence the collective cell migration modes. Our model can reproduce the fundamental features observed in experiments and highlight the role of mechanics in steering 3D collective cell dynamics during mammary acinar morphogenesis.

1. Introduction

Collective cell migration plays a central role in both physiological processes such as embryo development (Montell et al., 2012; Donà et al., 2013) and tissue repair (Poujade et al., 2007), and pathological processes including cancer metastasis (Alexander et al., 2008; Lin et al., 2017b). Diverse collective modes have been observed in, for instance, border cell migration during *Drosophila* oogenesis (Montell et al., 2012), lateral line migration during zebrafish organogenesis (Haas and Gilmour, 2006), and streaming migration of neural crest cells (Theveneau and Mayor, 2012). It is known that individual cells can actively migrate through an extension–attachment–contraction–detachment cyclic process (Lauffenburger and Horwitz, 1996). In cell aggregates, however, both cell–cell interactions (e.g., intercellular adhesion and movement coordination) and cell–environment interactions (e.g., mechanosensing of substrate geometry and stiffness) emerge as key regulators in their collective migration (Vedula et al., 2012; Doxzen et al., 2013; Garcia et al., 2015; Bi et al., 2016; Barton et al., 2017; Lin et al., 2017a; Xi et al., 2017). *In vitro* experiments have revealed that motile cells incubated on micropatterned substrate may rotate cohesively (Huang et al., 2005; Tate et al., 2015; Siedlik et al., 2017). Madin–Darby canine kidney cells seeded on an adhesive circular domain exhibit persistent collective rotation when the domain is small, whereas they orchestrate into dynamic local swirling when the domain is large enough (Doxzen et al., 2013). This indicates that environmental confinement plays a significant role in collective cell migration. A few *in silico* models have been provided to elucidate how these collective cell behaviors are coordinated in a two-dimensional (2D) space (Leong, 2013; Camley et al., 2014; Li and Sun, 2014; Xu et al., 2016; Lin et al., 2018).

Rotational motions are also common *in vivo* three-dimensional (3D) processes, such as cortical-cytoplasmic rotation of *Xenopus* egg during dorsal development (Gerhart et al., 1989) and cilia-driven rotation within the egg capsule of *Helisoma* embryos (Diefenbach et al., 1991). Virtually, *in vivo* collective cell migration often encounters 3D environmental constraints, as observed in the formation of ducts and acini in glandular tissues. Increasing experimental evidences indicate that rotational motion may be a fundamental feature of epithelial cells during tissue morphogenesis (Bianco et al., 2007; Haigo and Bilder, 2011; Tanner et al., 2012; Wang et al., 2013). Intriguingly, coherent angular motion (CAMo), a typical rotational mode observed in epithelium, has been found to be associated with 3D acinar morphogenesis (Fig. 1(a)), wherein cells form multicellular spheroids with a hollow lumen (Tanner et al., 2012; Wang et al., 2013). In addition, recent experiments also

* Corresponding author.
E-mail address: libome@tsinghua.edu.cn (B. Li).

https://doi.org/10.1016/j.jbiomech.2019.01.012
0021-9290/

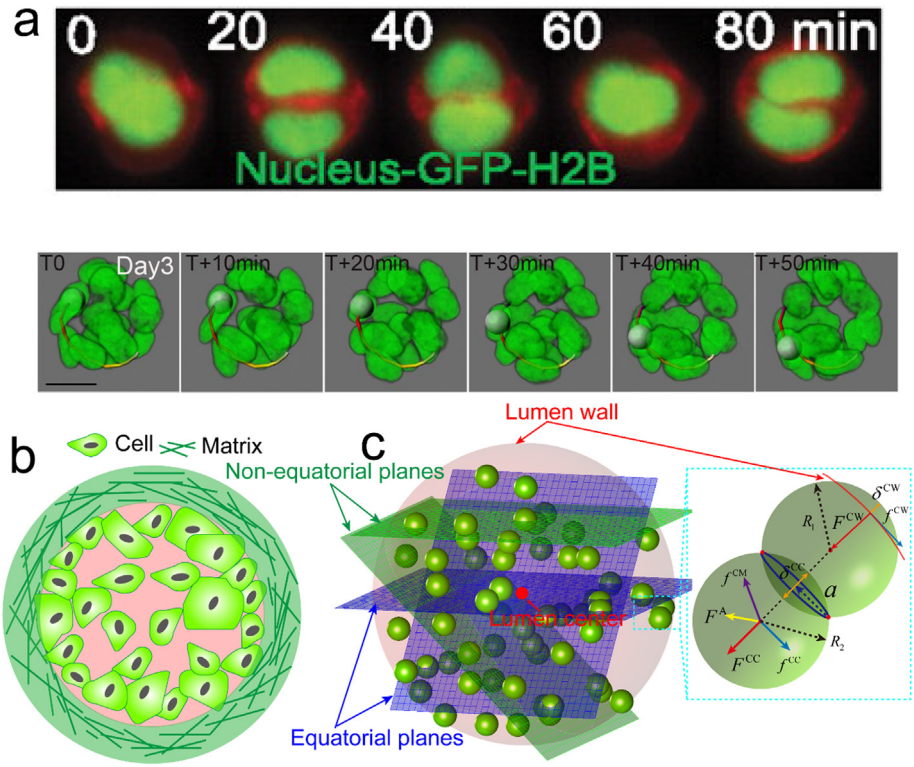

Fig. 1. (a) Experimental observation of coherent angular motions during mammary acinar morphogenesis in a 3D space. Upper row: S1-HMT3522 cells; lower row: MCF-10A cells. Reprinted from Refs (Tanner et al., 2012; Wang et al., 2013) with permission. (b) Schematic of a cell aggregate in a spherical acinus-like lumen. (c) Illustration of our model: cells are represented by small green spheres and the spherical lumen is shown in light red color; forces applied on interacting cells are elucidated in the dashed cyan box. (For interpretation of the references to color in this figure legend, the reader is referred to the web version of this article.)

showed that cells migrating on curved surfaces can detect out-of-plane curvatures. A high curvature may induce frequent cell detachments at the front edge of migrating cells and curvature-dependent migration velocity was observed on curved surfaces (Yevick et al., 2015; Xi et al., 2017). Although it has been recognized that geometrical constraints are essential for determining tissue-level polarity and embryogenesis in such migratory contexts, the mechanisms underpinning the emergence of rich 3D collective dynamics remain obscure (Gerhart et al., 1989; Diefenbach et al., 1991).

In this study, a cell-based model is developed to elucidate the prominent features of CAMo observed in an acinus-like lumen. Repulsion, adhesion and friction arising from cell–cell interactions and cell–lumen interactions, as well as active forces, are considered. We show that some novel migratory modes that are absent in 2D planar monolayers can emerge in a 3D space. These modes are found to be dictated by both cell persistence, random fluctuations, cell population, and cell density. Our model can not only capture primary features of CAMo of collective cells under 3D confinement and explain many previously reported experiments, but also predict some novel, testable collective cell dynamics.

2. Model

Consider a group of varied cell populations confined by a spherical acinus-like lumen, within which necessary liquid phase sustaining living cells is available (Fig. 1(b)). Unlike flat and polyhedral shape of cells cultured on a 2D substrate, cells in the 3D environment approximately exhibit spheroidal geometry. In our model, each cell is represented by a deformable sphere (Fig. 1(c)). At the cellular scale, cells move at a low Reynolds number, indicating that the effect of inertia can be neglected while the effect of viscosity is dominant (Ladoux and Mège, 2017). Considering the force balance of cell i (Fig. 1(c)), the motion equation can be described as

$$\mu \frac{\mathrm{d}\mathbf{r}_i}{\mathrm{d}t} = \mathbf{F}_{i,\mathrm{p}} + \mathbf{F}_{i,\mathrm{a}} + \mathbf{F}_{i,\mathrm{d}} \tag{1}$$

where $\mathbf{r}_i$ is the position of cell i; μ denotes the friction coefficient between cells and surrounding medium; $\mathbf{F}_{i,\mathrm{p}}$ is the passive force, which includes the force $\mathbf{F}_{ij}^{\mathrm{cc}}$ arising from cell–cell interactions and the force $\mathbf{F}_i^{\mathrm{cw}}$ from cell–lumen interactions; $\mathbf{F}_{i,\mathrm{a}}$ denotes active force of cell i; $\mathbf{F}_{i,\mathrm{d}}$ combines friction force between cells $\mathbf{f}_{ij}^{\mathrm{cc}}$ and that between cells and spherical lumen $\mathbf{f}_i^{\mathrm{cw}}$. These forces will be detailed below.

2.1. Passive force

Due to the contact with neighboring cells, a cell is subjected to passive forces arising from cell–cell elastic interaction and adhesion. On one hand, the cell is subjected to a repelling force from its contacting neighbors due to elastic compression. On the other hand, it also undergoes an adhesive force, which maintains cell–cell connection through adhesive proteins such as E-cadherins (Frixen et al., 1991). Here, we employ the Johnson–Kendall–Roberts (JKR) model (Johnson et al., 1971) to quantify the cell–cell interaction forces. Specifically, the JKR force acting on cell i, which arises from its contacting neighbor j, can be expressed as

$$\mathbf{F}_{ij}^{\mathrm{cc}} = F_{ij}^{\mathrm{cc}} \frac{\mathbf{r}_i - \mathbf{r}_j}{|\mathbf{r}_i - \mathbf{r}_j|}, \tag{2}$$

where F_{ij}^{cc} is the magnitude of the JKR force between cell i and j. It implicitly satisfies (Drasdo and Hoehme, 2012)

$$\delta_{ij} = \frac{2a_{ij}^2}{R} - \sqrt{\frac{4\pi\hat{\gamma}a_{ij}(1-\nu^2)}{E}},$$
$$a_{ij}^3 = \frac{3R(1-\nu^2)}{4E}\left[F_{ij}^{cc} + \frac{3\pi\hat{\gamma}R}{2} + \sqrt{3\pi\hat{\gamma}RF_{ij}^{cc} + \left(\frac{3\pi\hat{\gamma}R}{2}\right)^2}\right]. \quad (3)$$

Here, E, ν, and R are the elastic modulus, the Poisson's ratio, and the radius of cells, respectively; δ_{ij} is the sum of displacement due to deformation along the axis linking the centers of two cells; a_{ij} is the radius of contact region (Fig. 1(c)); $\hat{\gamma}$ denotes the adhesive surface energy between contacting cells (Drasdo and Hoehme, 2005, 2012).

We also adopt the JKR model to account for the interaction between cells and the spherical lumen wall. Accordingly, the cell i contacting the spherical lumen is subjected to a JKR force

$$\mathbf{F}_i^{cw} = F_i^{cw}\frac{\mathbf{r}_o - \mathbf{r}_i}{|\mathbf{r}_o - \mathbf{r}_i|} \quad (4)$$

along the direction $\frac{\mathbf{r}_o-\mathbf{r}_i}{|\mathbf{r}_o-\mathbf{r}_i|}$ coinciding with the radius of the lumen, where $\mathbf{r}_o$ indicates the position of the centroid of the spherical lumen. Here, the lumen centroid has been set as the origin of the reference frame. The magnitude F_i^{cw} is implicitly given as

$$\delta_i = \frac{a_i^2}{\bar{R}} - \sqrt{\frac{2\pi\hat{\gamma}_w a_i}{\bar{E}}},$$
$$a_i^3 = \frac{3\bar{R}}{4\bar{E}}\left[F_i^{cw} + 3\pi\hat{\gamma}_w\bar{R} + \sqrt{6\pi\hat{\gamma}_w\bar{R}F_i^{cw} + (3\pi\hat{\gamma}_w\bar{R})^2}\right], \quad (5)$$

where $\bar{R} = RR_w/(R_w - R)$ and $\bar{E}^{-1} = (1-\nu^2)E^{-1} + (1-\nu_w^2)E_w^{-1}$, with R_w, E_w, and ν_w denoting the radius, the elastic modulus, and the Poisson's ratio of the spherical lumen wall, respectively; $i \in \partial C$, with ∂C representing the set of cells contacting the spherical lumen; δ_i is the sum of displacement and a_i is the radius of contact region between cells and the lumen wall.

The total passive force applied on cell i can be written as

$$\mathbf{F}_{i,p} = \begin{cases} \mathbf{F}_i^{cw} + \sum_j \mathbf{F}_{ij}^{cc} & i \in \partial C, \\ \sum_j \mathbf{F}_{ij}^{cc} & i \notin \partial C, \end{cases} \quad (6)$$

where the summation is taken over all the neighboring cells of cell i.

2.2. Active force

To characterize the active motility of cells that stems from cell polarization, we introduce an active force,

$$\mathbf{F}_{i,a} = f_a\mathbf{n}_i, \quad (7)$$

where f_a is the magnitude that quantifies cell motility, and $\mathbf{n}_i$ is the direction of active force of cell i, i.e., the polarity vector of cell i. Considering cell persistence, which describes the tendency of cells to maintain their movement orientations (Selmeczi et al., 2005; Takagi et al., 2008; McCann et al., 2010; Li and Sun, 2014), the polarity vector $\mathbf{n}_i$ evolves as

$$\frac{d\mathbf{n}_i}{dt} = \alpha\left(\mathbf{n}_i \times \frac{\mathbf{v}_i}{|\mathbf{v}_i|}\right) \times \mathbf{n}_i + \beta\frac{\mathbf{n}_i \times \mathbf{m}_i}{|\mathbf{n}_i \times \mathbf{m}_i|}\xi, \quad (8)$$

where the first term on the right hand side characterizes cell persistence, and the second term corresponds to noise on cell reorientation. The vector $\mathbf{v}_i$ is the velocity of cell i; $\mathbf{m}_i$ is a random vector; ξ denotes unit-variance Gaussian white noise; α and β characterize the strength of cell persistence and noise, respectively.

2.3. Friction force

Cell motions in aggregates may experience friction forces from neighboring cells, extracellular matrix and spatial confinement. The friction force parallel to the contact surface is formulated as

$$\mathbf{f}_{ij}^{cc} = \mu^{cc}(\mathbf{I} - \mathbf{u}_{ij}\mathbf{u}_{ij}) \cdot (\mathbf{v}_j - \mathbf{v}_i), \quad (9)$$

where $\mathbf{I}$ is the unit tensor; $\mathbf{u}_{ij} = (\mathbf{r}_j - \mathbf{r}_i)/|\mathbf{r}_j - \mathbf{r}_i|$; μ^{cc} describes the friction coefficient (Drasdo and Hoehme, 2005, 2012).

Similarly, the friction force between a cell and the spherical lumen wall is calculated by

$$\mathbf{f}_i^{cw} = \mu^{cw}\left(\mathbf{I} - \frac{\mathbf{r}_o - \mathbf{r}_i}{|\mathbf{r}_o - \mathbf{r}_i|}\frac{\mathbf{r}_o - \mathbf{r}_i}{|\mathbf{r}_o - \mathbf{r}_i|}\right) \cdot (-\mathbf{v}_i), \quad (10)$$

where μ^{cw} is the friction coefficient between cells and the lumen wall and $i \in \partial C$. The total damping force can be written as

$$\mathbf{F}_{i,d} = \begin{cases} \mathbf{f}_i^{cw} + \sum_j \mathbf{f}_{ij}^{cc} & i \in \partial C, \\ \sum_j \mathbf{f}_{ij}^{cc} & i \notin \partial C, \end{cases} \quad (11)$$

where the summation is taken over all the neighboring cells around cell i.

3. Model setup and computation

We consider an aggregate with cell number N in a spherical lumen. At the initial state, the cells are distributed randomly. Take three basic parameters: the diameter of cells $L = 2R =$ 15 μm, the cell cycle $\tau = 4$ h, and the reference energy $F_T = 10^{-16}$ J, which is similar to the thermal energy K_BT in fluids and gases (Drasdo and Hoehme, 2005, 2012; Wang et al., 2013). We rescale the system by the length scale L, the time scale τ, and the force scale F_T/L. The dimensionless radius of the spherical lumen is defined by $\bar{R}_w = (N/4)^{1/3}$ to ensure the constant density, unless otherwise noted. To facilitate simulations, two dimensionless parameters are introduced: the dimensionless strength of cell persistence $\gamma = \alpha\tau$ and the dimensionless strength of noise $\eta = \beta\tau$. Table 1 shows the detailed model parameters and their typical values. The motion equations are solved by the explicit Euler method with a time step of 0.001. After each time step, the velocities of all cells are calculated and then their positions are updated. Generally, $\sim 1 \times 10^6$ time steps are needed for the system to reach a steady state. The calculations are performed in MATLAB.

4. Results and discussions

4.1. Two- and three-cell clusters

Experiments evidenced that during morphogenesis of mammary epithelial acini, 3D collective rotation of two or three cells may occur at the preliminary stage (Tanner et al., 2012; Wang et al., 2013). Motivated by these experiments, we now examine the migratory mode selection and dynamic features of two or three cells in a 3D acinus-like lumen.

To analyze the collective cell dynamics, all the cross-sections through the lumen centroid $\mathbf{r}_o$ are referred to as equatorial planes (blue planes in Fig. 1(c)), and other cross-sections not through the lumen centroid are referred to as non-equatorial planes (green planes in Fig. 1(c)). Cell motions with trajectories confined in the equatorial and non-equatorial planes are defined as the equatorial and non-equatorial modes, respectively. It can be found that after initial random walks, cells will move in a stable rotational manner (Fig. 2(a) and (b); Supplementary Movies 1 and 2. Furthermore, cells tend to rotate in the equatorial planes (Fig. 2(c) and (d)). Our results reproduce the CAMo during acinus formation observed in experiments (Tanner et al., 2012; Wang et al., 2013).

To quantify the rotational modes, we define the order parameter $g = |\langle(\mathbf{r}_i \times \mathbf{v}_i)/(|\mathbf{r}_i||\mathbf{v}_i|)\rangle|$, where $\langle\cdot\rangle$ stands for an average over all cells. For an ideal equatorial rotation, g is close to 1; while for random movement, g approaches 0. The distance which the

Table 1
Model parameters.

Parameter	Symbol	Unit	Value	Reference
Young's modulus of cells	E	Pa	450	Davidson et al. (1995)
Poisson's ratio of cells	ν		0.4	Mahaffy et al. (2000)
Interface energy between cells	$\hat{\gamma}$	J/m^2	10^{-4}	Drasdo and Hoehme (2012)
Magnitude of active force	f_a	nN	6.7	Assumed
Young's modulus of lumen wall	E_w	Pa	1000	Assumed
Poisson's ratio of matrix	ν		0.4	Assumed
Interface energy between cells and lumen wall	$\hat{\gamma}_w$	J/m^2	10^{-5}	Drasdo and Hoehme (2005)
Friction coefficient between cells and surrounding medium	μ	Ns/m	1	Assumed
Friction coefficient between cells	μ^{cc}	Ns/m	0.02	Assumed
Friction coefficient between cells and lumen wall	μ^{cw}	Ns/m	0.02	Assumed
Cell number	N		2–1000	Assumed
Radius of cells	R	μm	7.5	Drasdo and Hoehme (2005)
Cell cycle	τ	h	4	Tanner et al. (2012), Wang et al. (2013)
Time step	Δt	τ	0.001	

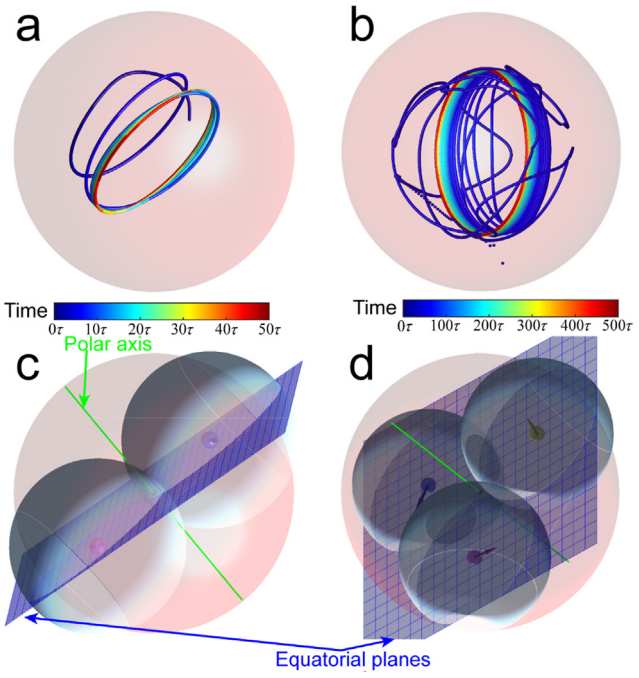

Fig. 2. Trajectories of a single cell in (a) two-cell and (b) three-cell systems. Snapshots of (c) two and (d) three cells rotating in a lumen at $t = 15\tau$ and $t = 500\tau$, respectively. Red spherical shell denotes the acinus-like lumen and cells are represented by grey balls. Small spheres are used to represent the centroid of cells and the colored arrows denote the migration direction. In all simulations, we take $\gamma = 1$ and $\eta = 0$. (For interpretation of the references to color in this figure legend, the reader is referred to the web version of this article.)

geometrical centroid of all cells deviates from the origin is calculated as $\rho_c = |\mathbf{r}_c|$, where $\mathbf{r}_c = (\sum_N \mathbf{r}_i)/N$. ρ_c reflects the spatial distribution of cells: $\rho_c \to 0$ means that cells distribute uniformly and exhibit spherical symmetry with regard to the origin in the lumen; otherwise ρ_c deviates from 0.

Fig. 3 shows the dynamic features of cell motions, where the strength of cell persistence γ is varied while noises are ignored. We find that for a two-cell system, with the increase of γ from 0 to 1, g increases from zero and finally reaches a plateau close to 1; while ρ_c increases to a high value rapidly at the beginning and then decays to zero (Fig. 3(a) and (b)). This behavior suggests that a robust equatorial rotation occurs and cells tend to distribute uniformly in the equatorial plane. Fig. 3(c) plots the instantaneous polar radius ρ of individual cells versus time. We find that with strong persistence $\gamma = 1$, ρ reaches a stationary value or slightly oscillates around a fixed value, indicating that all cells almost rotate around the origin in both two and three-cell systems.

We next examine how the cell persistence γ and the random fluctuation η affect cell migration. It reveals that large γ favors a robust rotation, while η tends to disfavor a steady rotation, as shown in Fig. 3(d). For given γ and η, a smaller system is easier to reach a steady rotation. To further quantify the parameter space allowing robust coherent rotation, we define a robust rotation by $g > 0.8$. Phase diagrams for the collective migration of two or three cells are established in Fig. 3(e) and (f), respectively. Intriguingly, the parameter boundary separating the regimes corresponding to robust rotation and random migration in the (γ, η) plane can be fitted by a proportional function. The boundary slope in the two-cell system is larger than that in the three-cell system, implying that stronger cell persistence is required to drive robust rotation in a larger system.

In addition, the behavior that cells tend to migrate in an equatorial plane can be explained from the force and energetic argument. The intersection area of an equatorial plane and the lumen is the largest one among all intersecting planes and thus can provide the largest space for accommodating cells. In other words, cells migrating in the equatorial planes exhibit less crowding. When cell motions deviate from the equatorial plane, they approach closer and stronger repelling forces may be generated, leading to a higher elastic energy in the system. Therefore, cells prefer to stay in the equatorial plane to release the compressive forces, and thus to reduce the total potential energy in the system.

4.2. Migratory modes of two- and three-cell systems

In Section 4.1, an equatorial rotation mode has been observed with γ spanning from 0 to 1 in a two-cell system. Here, we extend the parameter to a larger range. When γ ranges from 1 to 10, the equatorial rotation persists, as shown in Fig. 4(a) (Supplementary Movie 3). Increasing cell persistence strength (γ from 50 to 100) leads to cross-equatorial cell rotation, indicating that cells collectively enter different equatorial planes back and forth, as shown in dashed red box in Fig. 4(a) and (b) (Supplementary Movies 4–6). In this case, the spatial trajectories of cells form a stripe in space (Fig. 4(b)). Intriguingly, with enhanced cell persistence, the emerging stripe widens, indicating the amplitude of oscillating trajectories enlarges, while their period decreases, as further shown in Fig. 4(c). As γ increases further (e.g.,$\gamma = 300$), distinct non-equatorial rotations may emerge, where cells break away from the equatorial planes and rotate within a small domain in a non-equatorial plane (Fig. 4(a); Supplementary Movie 7). These results demonstrate that multiple novel rotational modes can be triggered by the strength of cell persistence, while random noises disturb rotation. In addition, our simulations predict that cells rotate 360°every 1.5 – 3 hours in both the two and three-cell systems,

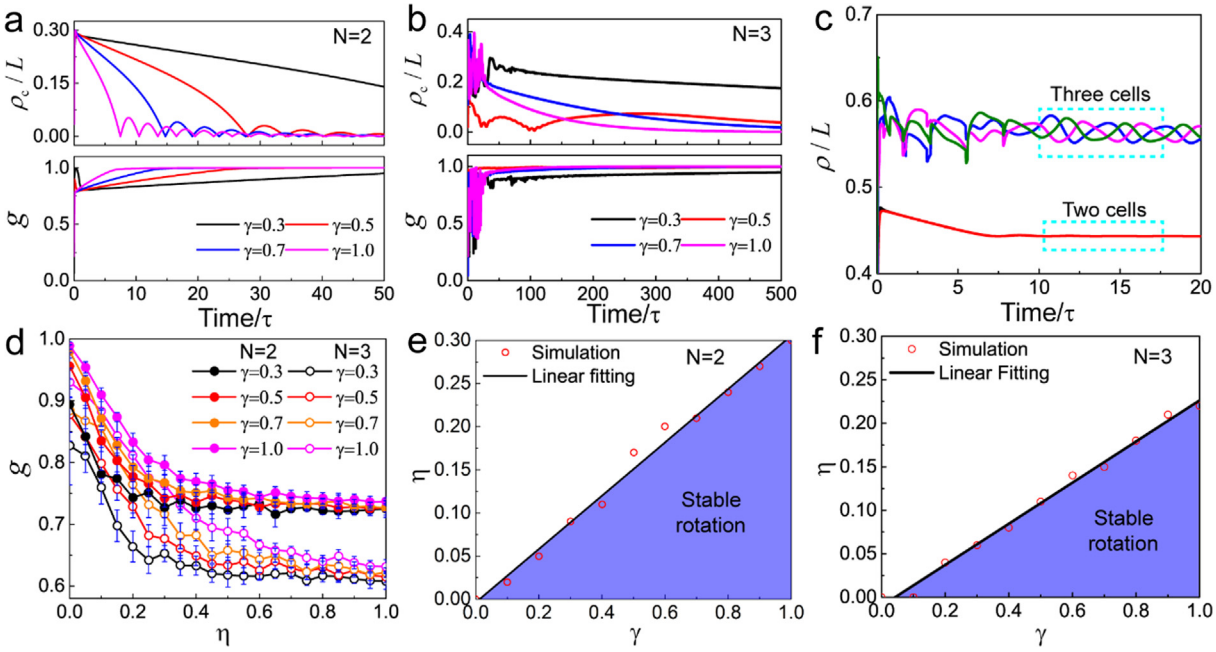

Fig. 3. Two and three cells rotating in a spherical acinus-like lumen. (a and b) The variation of the normalized distance ρ_c/L and the order parameter g under different cell persistence γ. (c) Polar radius of migrating cells for $\gamma = 1$. (d) Dependence of the order parameter g on γ and the strength of random fluctuation η. Phase diagrams of migration modes of (e) two cells and (f) three cells.

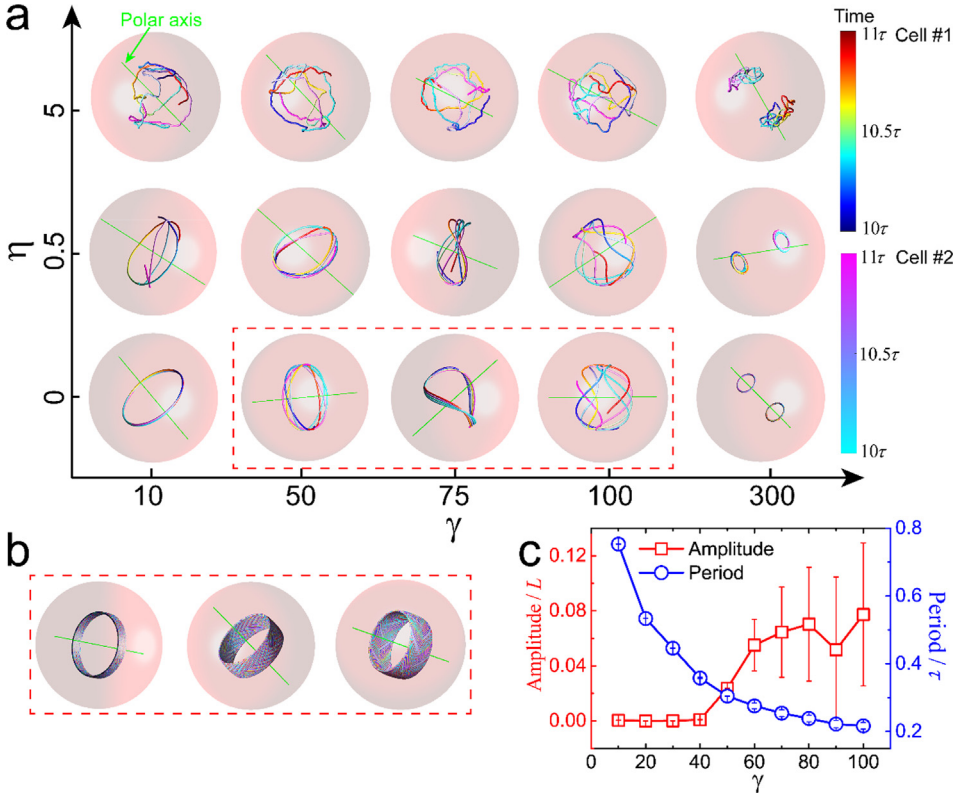

Fig. 4. (a) Rotational modes of two cells migrating in a spherical acinus-like lumen under different γ and η. Trajectories of two cells ranging from 10τ to 11τ are displayed. (b) Stripes formed by trajectories marked by the dashed box in (a) with time ranging from 10τ to 50τ. (c) The amplitude and period of oscillating trajectories versus γ, 20 independent simulations are performed for each case. Green line indicates the direction of polar axis defined by $\langle \sum_t (\mathbf{v}_i(t) \times \mathbf{v}_i(t+\Delta t))/|\sum_t (\mathbf{v}_i(t) \times \mathbf{v}_i(t+\Delta t))| \rangle$. (For interpretation of the references to color in this figure legend, the reader is referred to the web version of this article.)

in consistency with observed angular velocity of rotating cells during the early phase of acinus formation (Tanner et al., 2012; Wang et al., 2013). The rotational modes observed in Fig. 4 can be further characterized quantitatively by introducing the instant axis of rotation (see Supplementary Appendix 1 for details).

In a three-cell system, we observe similar rotational modes, as shown in Fig. 5 (Supplementary Movies 8–12). However, these rotational modes exhibit more complexity due to cell–cell interactions.

4.3. Migration modes of large cell clusters

During acinar morphogenesis, the cell number increases due to cell divisions (Tanner et al., 2012; Wang et al., 2013). In this subsection, we extend our model to see how large cell populations behave in a given 3D confinement. For example, we consider a system containing 1000 cells (Fig. 6). We notice that the migration of HaCaT cells in 2D context (Selmeczi et al., 2005) and HT1080 cells in 3D context (Wu et al., 2014) exhibits a persistence time spanning from 10 min to 2 h, which corresponds to the non-dimensional range $\gamma \in (2, 27.2)$ in our model. To focus on the role of cell persistence in regulating collective cell migration, we omit the noises and thus set $\eta = 0$. It can be seen that when γ is close to 0 (e.g., $\gamma = 0.1$), cells prefer to move to the periphery of the lumen and form a monolayer covering the whole wall surface (Fig. 6(a); Supplementary Movie 12). The velocity field suggests that cells rotate coherently while local cell–cell collision still occurs (Fig. 6(a2)). When cell persistence becomes stronger (e.g., $\gamma = 1$), cells aggregate to form a closed band and move in a twisted manner over the inner surface, referred to as *twisting band* (Fig. 6(b); Supplementary Movie 13). When γ increases further (e.g., $\gamma = 10$), the coordinated cells may form a rotating and looping band around the lumen equator, referred to as *circulating band*, as shown in Fig. 6(c) (Supplementary Movie 14). Continuously increasing cell persistence (e.g., $\gamma = 30$) can result in multilayer structures locally, referred to as *multilayer cluster* (Fig. 6(d); Supplementary Movie 15).

We introduce a spatial correlation function to gain insights into collective cell dynamics. It can determine the range over which cell migration is orchestrated and be expressed as

$$C(r) = \frac{\langle \delta \mathbf{v}_i \cdot \delta \mathbf{v}_j \rangle_{|r_{ij}-r| \leqslant \Delta r}}{\langle \delta \mathbf{v}_i \cdot \delta \mathbf{v}_i \rangle_{|r_{ij}-r| \leqslant \Delta r}}, \tag{12}$$

where $\delta \mathbf{v}_i = \mathbf{v}_i - \bar{\mathbf{v}}$ denotes the velocity fluctuation and Δr is a given separating length (Angelini et al., 2010). $\bar{\mathbf{v}}$ is the average velocity of all cells in the system. Besides, the overall angular velocity of the whole system is calculated by (Marmaras et al., 2010)

$$\langle \omega \rangle = \left\langle \arccos\left(\frac{\mathbf{r}_i(t) \cdot \mathbf{r}_i(t+\Delta t)}{|\mathbf{r}_i(t)| \cdot |\mathbf{r}_i(t+\Delta t)|} \right) \Big/ \Delta t \right\rangle. \tag{13}$$

Our results show that the correlation length, determined by the value where $C(r)$ reaches 0, increases sharply at the beginning and then falls down after the peak (inset in Fig. 7(a)), in consistency with the migration mode transition observed in Fig. 6. The overall angular velocity tends to increase with increasing individual cell persistence γ (Fig. 7(b)). With increasing γ, the overall centroid of total cells may gradually deviate from the origin, breaking the symmetry of the system (Fig. 7(c)). This behavior indicates that lumen formation during development may require an appropriate strength of cell persistence: too strong cell persistence would lead to unexpected configuration. Fig. 7(d) plots the order parameter g versus γ. It is found that with increasing γ, g undergoes a sharp increase at the beginning, and decreases gently after the peak value around 0.9, which is consistent with the trend of correlation length. This behavior suggests that a perfect lumen is prone to form when cell persistence is moderate (e.g.$\gamma \sim 3.0$).

Experimental observations have revealed that tissue polarity regulated by Akt and Rac1 pathways is closely associated with the formation of CAMo and acini (Tanner et al., 2012). Akt and Rac1 switches are known to be crucial for maintaining directionally persistent cell migration (Pankov et al., 2005; Tanner et al., 2012). These results suggest that cell persistence is indispensable for CAMo during lumen formation. There exists an appropriate or optimal range of γ for sustaining a stable CAMo and robust lumen formation, in qualitative agreement with the above experiments.

4.4. Effects of cell density

Now we consider the role of cell density playing in collective cell migration. Since our system is spherical and the cell density depends on the ratio between the cell number and the volume of the lumen, the lumen's curvature commonly entangles the cell density. To distinguish the effects of cell density and lumen curvature, we identify the effects of cell density through three cases: (i) a varied lumen radius but constant cell population (Fig. 8(a)–(d)), (ii) a varied lumen radius but a constant cell density (Fig. 8(e)–(g)), and (iii) a fixed lumen radius but increasing cell population (Fig. 8(h) and (i)). We take the typical situation with relatively strong cell persistence ($\gamma = 10$) as an example. In this case, the system tends to evolve into a dynamic band structure, as shown in Fig. 6(c).

For Case (i) containing 1000 cells, when the radius shrinks (equivalently, the cell density increases), the band structure transitions to a *polar vortex*, where cells rotate around a polar axis and even fulfill the whole lumen instead of forming a band, as shown in Fig. 8(a) (Sknepnek and Henkes, 2015). When the lumen radius is large (e.g., $\bar{R}_w \geqslant 9$), the band structure may break and several isolated clusters emerge (Fig. 8(c) and (d); Supplementary Movies 16 and 17). For Case (ii), with the cell number increasing from 250 to 1000, the band structure maintains while its width increases,

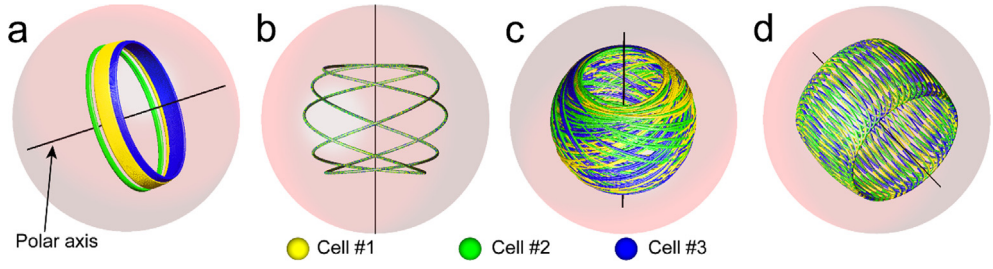

Fig. 5. Rotational modes of three cells migrating in a spherical acinus-like lumen. (a) $\gamma = 10$; (b) $\gamma = 50$; (c) $\gamma = 100$; (d) $\gamma = 300$. Different cells are labelled by yellow, green and blue, respectively. Polar axis is shown in black line. In all simulations, time ranges from 10τ to 50τ. (For interpretation of the references to color in this figure legend, the reader is referred to the web version of this article.)

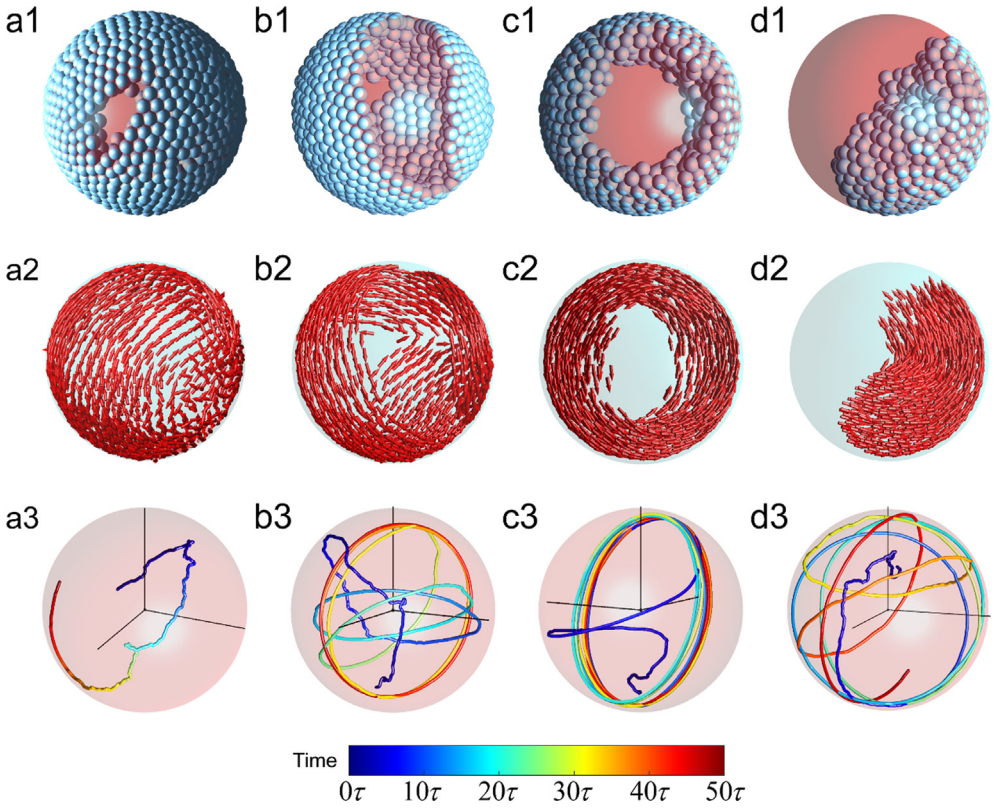

Fig. 6. Simulation snapshots of 1000 cells migrating in a spherical acinus-like lumen at $t = 50\tau$. (a) $\gamma = 0.1$; (b) $\gamma = 1$; (c) $\gamma = 10$; (d) $\gamma = 30$. Upper row: position of cells in lumen; middle row: velocity direction of cells; lower row: trajectory of a single cell (randomly chosen in the whole system).

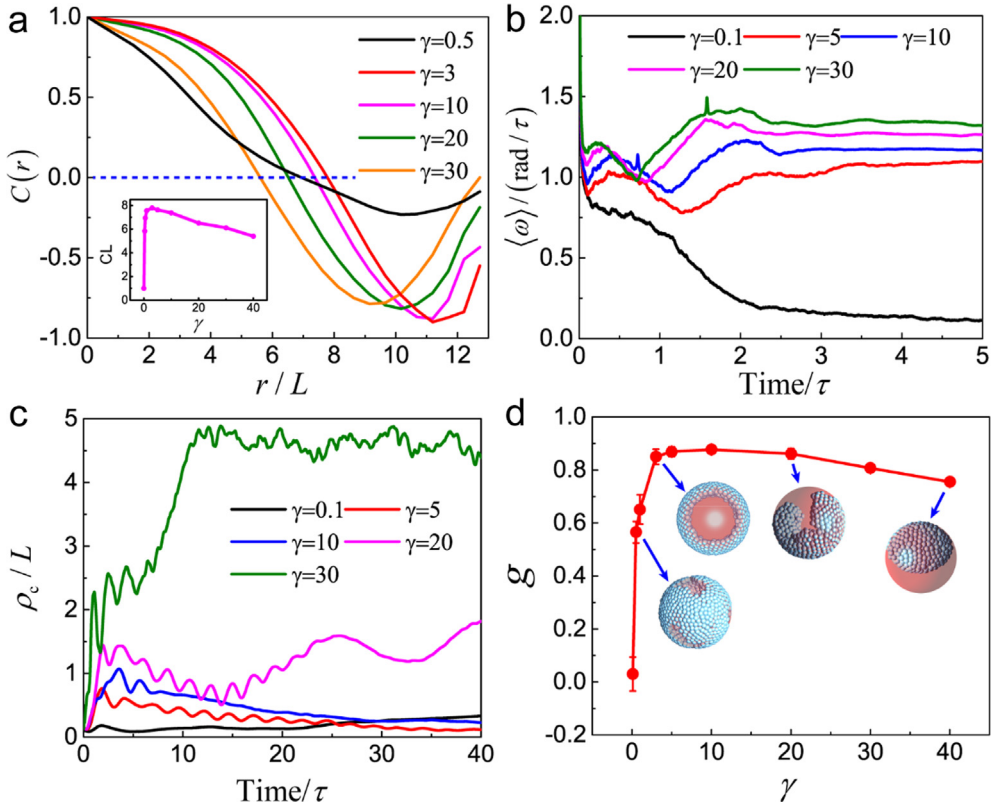

Fig. 7. (a) Spatial correlation function of velocity. Inset: correlation length versus γ. (b) Average angular velocity of migrating cells. (c) The distance ρ_c/L that the overall centroid of cells deviates from the center of the acinus-like lumen. (d) Dependence of the order parameter g on the variation of γ, where 10 trials are performed for each case.

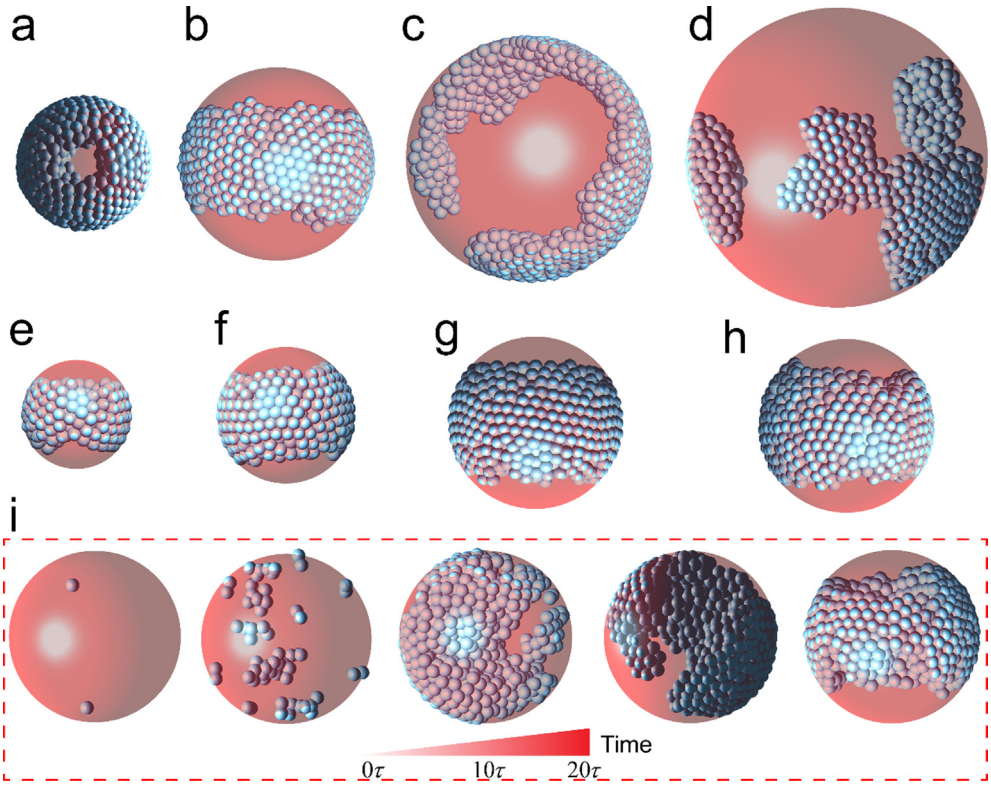

Fig. 8. Rotational patterns varied with cell population and the radius of the spatial confinement. (a) $N = 1000$, $\bar{R}_w = 5$; (b) $N = 1000$, $\bar{R}_w = 7$; (c) $N = 1000$, $\bar{R}_w = 9$; (d) $N = 1000$, $\bar{R}_w = 11$; (e) $N = 250$, $\bar{R}_w = 4$; (f) $N = 500$, $\bar{R}_w = 5$; (g) $N = 1000$, $\bar{R}_w = 6.3$; (h) Rotational pattern considering cell proliferation; $N = 1024$, $\bar{R}_w = 6.3$; (i) Evolution of the migration modes during cell proliferation. In all simulations, we take $\gamma = 10$ and $\eta = 0$.

indicating that surface curvature does not affect the migration mode remarkably under a constant cell density in the considered spherical system. For Case (iii), we increase the cell number from 2 to 1024 (Fig. 8(h) and (i); Supplementary Movie 18). Within a constant cell cycle τ, a cell divides into two daughter cells separated by a small distance. Comparison with Fig. 8(g) shows that the dividing process *per se* has an insignificant influence on the final steady state (Fig. 8(h)). However, the variation of cell density due to proliferation can significantly affect their migration mode (Fig. 8(i)). These behaviors reveal that cell density plays a key role in regulating CAMo and thus in lumen formation. Experiments showed that the radius of basement membrane enlarges with the cell number during morphogenesis of mammary epithelial acini (Wang et al., 2013). Maintaining a specified cell density may be a developmental strategy to ensure robust CAMo during lumen formation *in vivo*, which deserves further experimental validation.

5. Conclusions

A cell-based model has been proposed to study the 3D CAMo observed in experiments. We show that cell dynamics exhibits distinct features in multicellular systems with different population scale. The migratory modes of equatorial rotation, cross-equatorial rotation and non-equatorial rotation are found in a two-cell system, while the rotational modes in a three-cell system are more sophisticated due to more frequent cell–cell coordination. In a larger system, *twisting band*, *circulating band* and *multilayer cluster* may emerge. The emergence of these modes and their transitions are regulated by the population, persistence and density of cells. This study holds potential significance in various biological processes, such as tissue morphogenesis, wound healing, and active swimming.

Though only a spherical acinus-like lumen has been considered in the present paper, our model can be applied to systems of other shapes, such as cylindrical lumens, which are common during duct morphogenesis. In this case, the effect of local curvature should be considered on the interaction between cells and the lumen wall.

Conflict of interest

The authors declare that they have no conflict of interest associated with the presented work.

Acknowledgements

Supports from National Natural Science Foundation of China (Grant Nos. 11620101001, 11672161, and 11432008), Tsinghua University (20151080441), and the Thousand Young Talents Program of China are acknowledged.

Appendix A. Supplementary material

Supplementary data to this article can be found online at https://doi.org/10.1016/j.jbiomech.2019.01.012.

References

Alexander, S., Koehl, G.E., Hirschberg, M., Geissler, E.K., Friedl, P., 2008. Dynamic imaging of cancer growth and invasion: a modified skin-fold chamber model. Histochem. Cell Biol. 130, 1147–1154.

Angelini, T.E., Hannezo, E., Trepat, X., Fredberg, J.J., Weitz, D.A., 2010. Cell migration driven by cooperative substrate deformation patterns. Phys. Rev. Lett. 104, 168104.

Barton, D.L., Henkes, S., Weijer, C.J., Sknepnek, R., 2017. Active Vertex Model for cell-resolution description of epithelial tissue mechanics. PLoS Comp. Biol. 13, e1005569.

Bi, D., Yang, X., Marchetti, M.C., Manning, M.L., 2016. Motility-driven glass and jamming transitions in biological tissues. Phys. Rev. X 6, 021011.
Bianco, A., Poukkula, M., Cliffe, A., Mathieu, J., Luque, C.M., Fulga, T.A., Rørth, P., 2007. Two distinct modes of guidance signalling during collective migration of border cells. Nature 448, 362–365.
Camley, B.A., Zhang, Y., Zhao, Y., Li, B., Ben-Jacob, E., Levine, H., Rappel, W.-J., 2014. Polarity mechanisms such as contact inhibition of locomotion regulate persistent rotational motion of mammalian cells on micropatterns. PNAS 111, 14770–14775.
Davidson, L.A., Koehl, M., Keller, R., Oster, G.F., 1995. How do sea urchins invaginate? Using biomechanics to distinguish between mechanisms of primary invagination. Development 121, 2005–2018.
Diefenbach, T.J., Koehncke, N.K., Goldberg, J.I., 1991. Characterization and development of rotational behavior in Helisoma embryos: role of endogenous serotonin. Dev. Neurobiol. 22, 922–934.
Donà, E., Barry, J.D., Valentin, G., Quirin, C., Khmelinskii, A., Kunze, A., Durdu, S., Newton, L.R., Fernandez-Minan, A., Huber, W., 2013. Directional tissue migration through a self-generated chemokine gradient. Nature 503, 285–289.
Doxzen, K., Vedula, S.R.K., Leong, M.C., Hirata, H., Gov, N.S., Kabla, A.J., Ladoux, B., Lim, C.T., 2013. Guidance of collective cell migration by substrate geometry. Integr. Biol. 5, 1026–1035.
Drasdo, D., Hoehme, S., 2005. A single-cell-based model of tumor growth in vitro: monolayers and spheroids. Phys. Biol. 2, 133.
Drasdo, D., Hoehme, S., 2012. Modeling the impact of granular embedding media, and pulling versus pushing cells on growing cell clones. New J. Phys. 14, 055025.
Frixen, U.H., Behrens, J., Sachs, M., Eberle, G., Voss, B., Warda, A., Löchner, D., Birchmeier, W., 1991. E-cadherin-mediated cell-cell adhesion prevents invasiveness of human carcinoma cells. J. Cell Biol. 113, 173–185.
Garcia, S., Hannezo, E., Elgeti, J., Joanny, J.-F., Silberzan, P., Gov, N.S., 2015. Physics of active jamming during collective cellular motion in a monolayer. PNAS 112, 15314–15319.
Gerhart, J., Danilchik, M., Doniach, T., Roberts, S., Rowning, B., Stewart, R., 1989. Cortical rotation of the Xenopus egg: consequences for the anteroposterior pattern of embryonic dorsal development. Development 107, 37–51.
Haas, P., Gilmour, D., 2006. Chemokine signaling mediates self-organizing tissue migration in the zebrafish lateral line. Dev. Cell 10, 673–680.
Haigo, S.L., Bilder, D., 2011. Global tissue revolutions in a morphogenetic movement controlling elongation. Science 331, 1071–1074.
Huang, S., Brangwynne, C., Parker, K., Ingber, D., 2005. Symmetry-breaking in mammalian cell cohort migration during tissue pattern formation: Role of random-walk persistence. Cytoskeleton 61, 201–213.
Johnson, K., Kendall, K., Roberts, A., 1971. Surface energy and the contact of elastic solids. Proc. R. Soc. Lond. A 324, 301–313.
Ladoux, B., Mège, R.-M., 2017. Mechanobiology of collective cell behaviours. Nat. Rev. Mol. Cell Biol. 18, 743.
Lauffenburger, D.A., Horwitz, A.F., 1996. Cell migration: a physically integrated molecular process. Cell 84, 359–369.
Leong, F.Y., 2013. Physical explanation of coupled cell-cell rotational behavior and interfacial morphology: A particle dynamics model. Biophys. J. 105, 2301–2311.
Li, B., Sun, S.X., 2014. Coherent motions in confluent cell monolayer sheets. Biophys. J. 107, 1532–1541.
Lin, S.Z., Li, B., Lan, G., Feng, X.Q., 2017a. Activation and synchronization of the oscillatory morphodynamics in multicellular monolayer. PNAS 114, 8157–8162.
Lin, S.Z., Li, B., Xu, G.K., Feng, X.Q., 2017b. Collective dynamics of cancer cells confined in a confluent monolayer of normal cells. J. Biomech. 52, 140–147.
Lin, S.Z., Xue, S.L., Li, B., Feng, X.Q., 2018. An oscillating dynamic model of collective cells in a monolayer. J. Mech. Phys. Solids 112, 650–666.
Mahaffy, R., Shih, C., MacKintosh, F., Käs, J., 2000. Scanning probe-based frequency-dependent microrheology of polymer gels and biological cells. Phys. Rev. Lett. 85, 880.
Marmaras, A., Berge, U., Ferrari, A., Kurtcuoglu, V., Poulikakos, D., Kroschewski, R., 2010. A mathematical method for the 3D analysis of rotating deformable systems applied on lumen-forming MDCK cell aggregates. Cytoskeleton 67, 224–240.
McCann, C.P., Kriebel, P.W., Parent, C.A., Losert, W., 2010. Cell speed, persistence and information transmission during signal relay and collective migration. J. Cell Sci. 123, 1724–1731.
Montell, D.J., Yoon, W.H., Starz-Gaiano, M., 2012. Group choreography: mechanisms orchestrating the collective movement of border cells. Nat. Rev. Mol. Cell Biol. 13, 631–645.
Pankov, R., Endo, Y., Even-Ram, S., Araki, M., Clark, K., Cukierman, E., Matsumoto, K., Yamada, K.M., 2005. A Rac switch regulates random versus directionally persistent cell migration. J. Cell Biol. 170, 793–802.
Poujade, M., Grasland-Mongrain, E., Hertzog, A., Jouanneau, J., Chavrier, P., Ladoux, B., Buguin, A., Silberzan, P., 2007. Collective migration of an epithelial monolayer in response to a model wound. PNAS 104, 15988–15993.
Selmeczi, D., Mosler, S., Hagedorn, P.H., Larsen, N.B., Flyvbjerg, H., 2005. Cell motility as persistent random motion: theories from experiments. Biophys. J. 89, 912–931.
Siedlik, M.J., Manivannan, S., Kevrekidis, I.G., Nelson, C.M., 2017. Cell division induces and switches coherent angular motion within bounded cellular collectives. Biophys. J. 112, 2419–2427.
Sknepnek, R., Henkes, S., 2015. Active swarms on a sphere. Phys. Rev. E 91, 022306.
Takagi, H., Sato, M.J., Yanagida, T., Ueda, M., 2008. Functional analysis of spontaneous cell movement under different physiological conditions. PLoS One 3, e2648.
Tanner, K., Mori, H., Mroue, R., Bruni-Cardoso, A., Bissell, M.J., 2012. Coherent angular motion in the establishment of multicellular architecture of glandular tissues. PNAS 109, 1973–1978.
Tate, S., Imai, M., Matsushita, N., Nishimura, E.K., Higashiyama, S., Nanba, D., 2015. Rotation is the primary motion of paired human epidermal keratinocytes. J. Dematol. Sci. 79, 194–202.
Theveneau, E., Mayor, R., 2012. Neural crest migration: interplay between chemorepellents, chemoattractants, contact inhibition, epithelial–mesenchymal transition, and collective cell migration. WIRs Dev. Biol. 1, 435–445.
Vedula, S.R.K., Leong, M.C., Lai, T.L., Hersen, P., Kabla, A.J., Lim, C.T., Ladoux, B., 2012. Emerging modes of collective cell migration induced by geometrical constraints. PNAS 109, 12974–12979.
Wang, H., Lacoche, S., Huang, L., Xue, B., Muthuswamy, S.K., 2013. Rotational motion during three-dimensional morphogenesis of mammary epithelial acini relates to laminin matrix assembly. PNAS 110, 163–168.
Wu, P.-H., Giri, A., Sun, S.X., Wirtz, D., 2014. Three-dimensional cell migration does not follow a random walk. Proc Natl. Acad. Sci. U.S.A., 201318967
Xi, W., Sonam, S., Saw, T.B., Ladoux, B., Lim, C.T., 2017. Emergent patterns of collective cell migration under tubular confinement. Nat. Commun. 8, 1517.
Xu, G.K., Liu, Y., Zheng, Z., 2016. Oriented cell division affects the global stress and cell packing geometry of a monolayer under stretch. J. Biomech. 49, 401–407.
Yevick, H.G., Duclos, G., Bonnet, I., Silberzan, P., 2015. Architecture and migration of an epithelium on a cylindrical wire. PNAS 112, 5944–5949.